Kinematic Oscillations of Post-CME Blobs Detected by K-Cor on 2017 September 10

Jae-Ok Lee[1], Kyung-Suk Cho[1,2], Valery M. Nakariakov[3,4], Harim Lee[3], Rok-Soon Kim[1],
Soojeong Jang[1], Heesu Yang[1], Sujin Kim[1], and Yeon-Han Kim[1]

[1]Korea Astronomy and Space Science Institute, Daejeon 34055, Korea; ljoking@kasi.re.kr
[2]University of Science and Technology, Daejeon 34055, Korea
[3]School of Space Research, Kyung Hee University, Yongin-si 17104, Korea
[4]Centre for Fusion, Space and Astrophysics Department of Physics, University of Warwick, Coventry CV4 7AL, UK

Abstract: We investigate 20 post-coronal mass ejection (CME) blobs formed in the post-CME current sheet (CS) that were observed by K-Cor on 2017 September 10. By visual inspection of the trajectories and projected speed variations of each blob, we find that all blobs except one show irregular "zigzag" trajectories resembling transverse oscillatory motions along the CS, and have at least one oscillatory pattern in their instantaneous radial speeds. Their oscillation periods are ranging from 30 to 91 s and their speed amplitudes from 128 to 902 km s^{-1}. Among 19 blobs, 10 blobs have experienced at least two cycles of radial speed oscillations with different speed amplitudes and periods, while 9 blobs undergo one oscillation cycle. To examine whether or not the apparent speed oscillations can be explained by vortex shedding, we estimate the quantitative parameter of vortex shedding, the Strouhal number, by using the observed lateral widths, linear speeds, and oscillation periods of the blobs. We then compare our estimates with theoretical and experimental results from MHD simulations and fluid dynamic experiments. We find that the observed Strouhal numbers range from 0.2 to 2.1, consistent with those (0.15–3.0) from fluid dynamic experiments of bluff spheres, while they are higher than those (0.15–0.25) from MHD simulations of cylindrical shapes. We thus find that blobs formed in a post-CME CS undergo kinematic oscillations caused by fluid dynamic vortex shedding. The vortex shedding is driven by the interaction of the outward-moving blob having a bluff spherical shape with the background plasma in the post-CME CS.

Key words: Sun: corona — Sun: coronal mass ejections (CMEs) — Sun: oscillations — hydrodynamics — magnetohydrodynamics (MHD)

1. Introduction

Coronal mass ejections (CMEs) are explosive phenomena occurring in the solar corona that expel huge amounts of coronal material and magnetic fields into interplanetary space. After a CME erupts, occasionally new narrow bright coronal ray structures develop in the wake of the CME, and outward-moving localized bright structures along the coronal rays are observed by ground coronagraphs (e.g., the COronal Solar Magnetism Observatory (COSMO) K-coronagraph (K-Cor) on the Mauna Loa Solar Observatory) and spaceborne coronagraphs (e.g., Large Angle Spectroscopic COronagraph (LASCO; Brueckner et al. 1995) C2 and C3 on board the Solar and Heliospheric Observatory (SOHO) spacecraft and Sun Earth Connection Coronal and Heliospheric Investigation (SECCHI; Howard et al. 2008) COR-2 on board the Solar TErrestrial RElations Observatory (STEREO) spacecraft). These kinds of coronal ray and outward-moving localized bright structures are called post-CME rays and post-CME blobs.

From examining post-CME rays with coronagraphs and/or extreme ultraviolet (EUV) telescopes, various studies identified post-CME rays with post-CME current sheets (CSs) because they are likely to connect post flare loops with the trailing edge of the CME flux rope, and their observed structures are similar to those from the erupting CME flux rope model developed by Lin & Forbes (2000) (Webb et al. 2003; Ko et al. 2003; Lin et al. 2005; Ling et al. 2014; Lin et al. 2015; Cheng et al. 2018). From post-CME blob observations (Ko et al. 2003; Lin et al. 2005; Vršnak et al. 2009; Song et al. 2012; Kwon et al. 2016; Webb & Vourlidas 2016; Chae et al. 2017; Cheng et al. 2018; Lee et al. 2020; Yu et al. 2020), multiple studies find the following characteristics: (1) Post-CME blobs are observed in or along the post-CME CSs. (2) They have elongated structures parallel to the CSs. (3) They move outward with average linear speeds 38–1075 km s^{-1} during their propagation and they undergo average accelerations from -1.4 to 14.5 km s^{-2}. Because of these characteristics, it is expected that post-CME blobs can be generated by magnetic reconnection triggered by the tearing mode instability in the Sweet-Parker CS (Furth et al. 1963; Shibata, & Tanuma 2001; Shen et al. 2011).

In order to identify possible formation mechanisms of post-CME blobs, resistivity magnetohydrodynamic (MHD) simulations are used (Riley et al. 2007; Shen et

---

al. 2011; Mei et al. 2012; Takahashiet al. 2017). Such studies commonly accept that the post-CME blobs are generated by magnetic reconnection triggered by the tearing mode instability in the Sweet-Parker CSs. Their kinematics are mainly driven from reconnection outflows generated by the magnetic reconnection processes near the magnetic X-points in the CSs. In addition to that, with a high resolution MHD simulation, Mei et al. (2012) examine the velocity distributions of the plasma inside and outside of a post-CME blob in a CS as shown in their Figure 12. They show the existence of a velocity distribution discontinuity between the interior and the exterior of the post-CME blob, and report that the blob drives the plasma ahead of it outward and depletes the plasma behind of it while the plasma inside the blob is moving outward. The void is filled by the local plasma moving towards the CS. This finding suggests that the complex flow patterns inside and outside of post-CME blobs in the CS are one type of turbulence, which may cause the broadening of the CS. The post-CME blobs appear to have specific velocities which are higher than the background plasma velocities.

It is well known that a Kelvin-Helmholtz instability (KHI) occurs at velocity shear regions in a single continuous fluid (e.g., the waving motion of a flag in a wind) or the interface of two fluids (e.g., surface waves at the air–sea interface). The KHI can generate vortex motions. In the first case, the interaction between a flow and an obstacle in the fluid could generate vortex motions behind the obstacle. The vortex motions are produced periodically by opposite vorticity from the two sides of the obstacle and their drag by the flow (Tritton 1977; Williamson 1996). This hydrodynamic phenomenon is referred to as Kármán vortex street or vortex shedding. Vortex shedding is numerically expected in the MHD regime in the solar corona (e.g., buoyant magnetic flux tubes (Emonet et al. 2001), coronal loops (Gruszecki et al. 2010), and CME eruptions (Syntelis, & Antolin 2019)). Hereafter, we adopt Alfvénic vortex shedding to explain the vortex shedding in the MHD regime (Gruszecki et al. 2010). Interestingly, Emonet et al. (2001) show that the Alfvénic vortex shedding can cause "zigzag" motions of the buoyant magnetic flux tubes, which can be observed as radial speed oscillations: the actual oscillations are transverse in the direction perpendicular to the direction of the erupting tubes, as the back-reaction of the vortices shed from the alternate sides of the tubes. The transverse oscillations may appear to be in the radial direction due to projection effects, if the line of sight has a not-right angle to the vector of the trajectory. In addition, several studies conclude that Alfvénic vortex shedding can attribute to the radial speed oscillations of CMEs (Lee et al. 2015), the excitation of kink oscillations of solar coronal loops (Nakariakov et al. 2009), and swaying motions observed in comet tails (Nistico et al. 2018) and in hot coronal jets (Samanta et al. 2019).

Based on the above findings, we speculate that in post-CME CS Alfvénic vortex shedding can be generated by the interaction between post-CME blobs and back-

ground plasma. The interaction can cause kinematic oscillations of post-CME blobs while they propagate. Since the outward-moving post-CME blobs move parallel or anti-parallel to magnetic field lines, the magnetic fields do not suppress vortex motions generated by the post-CME blobs. This indicates that the post-CME CS can provide the conditions required for generating the Alfvénic vortex shedding. To our knowledge, there are no observational reports of kinematic oscillations, "zigzag" motions with radial speed oscillations, of post-CME blobs until now. In this study, we investigate 20 post-CME blobs formed in the post-CME CS observed by K-Cor on 2017 September 10, and examine whether (1) there exist kinematic oscillations and (2) their generation is related to the vortex shedding or not.

This paper is organized as follows. In Section 2, we describe the data and the analyses for the determination of speed oscillations and their observational parameters. We provide our results in Section 3. A brief summary and discussion are presented in Section 4.

2. Data and Analysis

2.1. Data

For the data selection, we use the following procedure: (1) We investigate post-CME blobs along or in the post-CME CS after the eruption of a CME (Cheng et al. 2018; Gary et al. 2018; Gopalswamy et al. 2018; Liu et al. 2018; Longcope et al. 2018; Warren et al. 2018; Liu et al. 2019; Lee et al. 2020). (2) By visual inspection of K-Cor and LASCO-C2 intensity, and their running difference images, we try to find localized brightness-enhanced structures. When such structures are identified in three or more consecutive images of K-Cor or LASCO-C2 as outward moving, we select them as candidate of K-Cor or LASCO-C2 blobs. The search process for the K-Cor (LASCO-C2) blobs as well as their observation heights are well described in the Section 2 of Lee et al. (2020) (hereafter Paper I). During the period from 16:36 to 18:56 UT, we find 34 K-Cor blobs and 4 LASCO-C2 blobs. (3) Among them, we consider 25 K-Cor blobs with at least 7 height-time data points, which allows us to make at least six-point speed-time profiles and to determine the kinematics of post-CME blobs with a reasonable accuracy. (4) Finally, we use 20 blobs that appeared in the post-CME CS because the kinematic motions of blobs in and above the CS are different (as described in Paper I): Group 1 (blobs in the CS) has a wide range of speeds (38–945 km s^{-1}) and speeds tend to increase with height, with heights ranging from 1.17 to 1.82 $R_{\rm Sun}$, while Group 2 (blobs above the CS) has a narrow speed range (579–726 km s^{-1}) and speeds are constant with height from 1.57 to 2.31 $R_{\rm Sun}$. The height-time data of the 20 blobs are taken from Figure 3 of Paper I. We only consider height-time data of the local maximum brightness of each blob to study the kinematic oscillations of the blobs and their possible generation mechanisms. The K-Cor images are taken from the
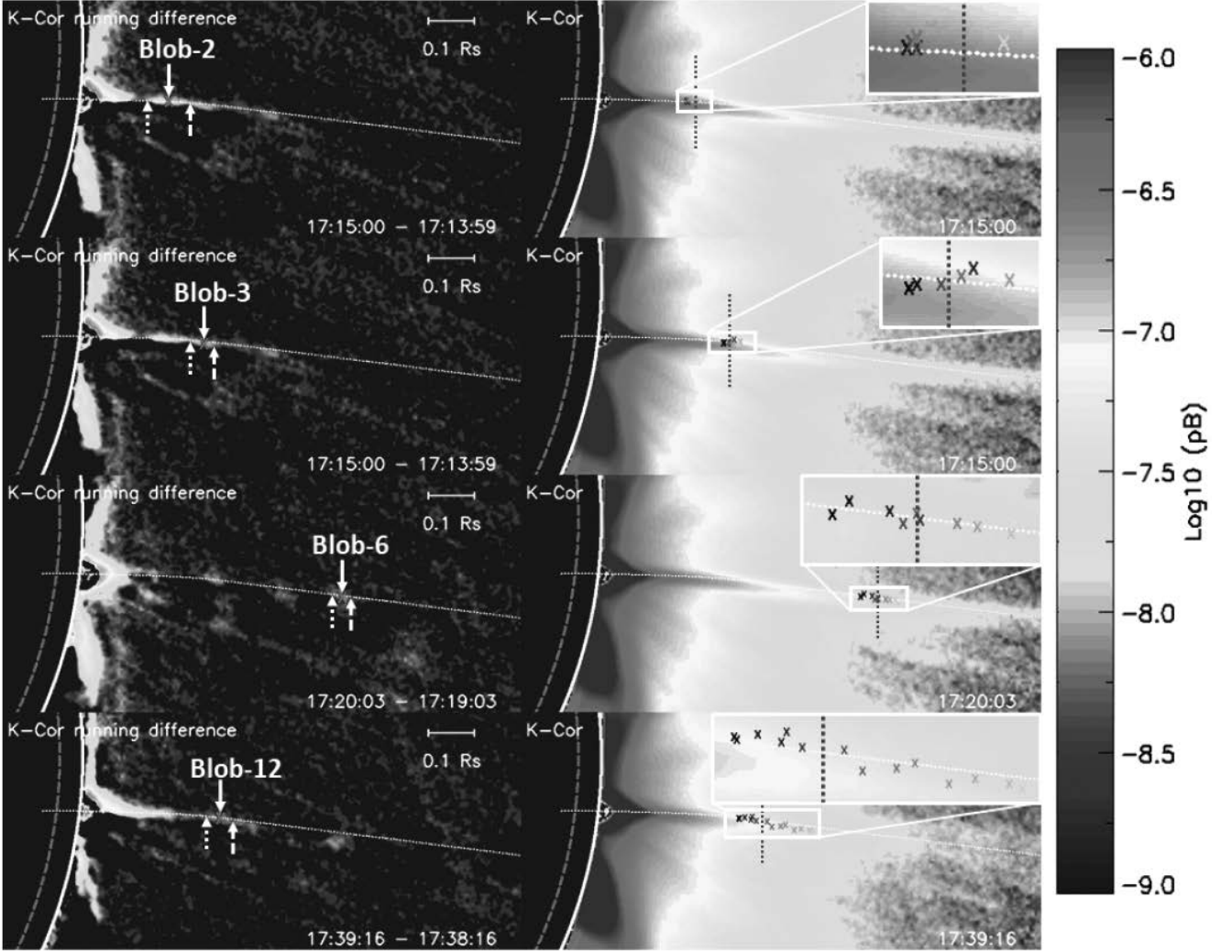
Figure 1. Examples of K-Cor blobs in a post-CME CS, observed on 2017 September 10 at 17:15:00, 17:20:03, and 17:39:16 UT in K-Cor running difference images (left column). Their trajectories (black and light-gray cross symbols) are shown on K-Cor intensity images (right column). Zoom-in images of the blob motions are shown in the white boxes. "Blob-2", "Blob-3", "Blob-6", and "Blob-12" denote the K-Cor blobs. In the panels on the left, white arrows with red cross symbols, dashed arrows, and dotted arrows show the local maximum brightness, front edge, and trailing edge of each blob, respectively. White dotted lines indicate the general propagation directions. In the panels on the right, black and light-gray cross symbols indicate the locations of the first and last appearance of the local maximum brightness, respectively. The purple dotted lines mark the cuts used for the space-time plots in Figure 5. All K-Cor images are cut such that XCEN and YCEN are $1390''$ and $-155''$, respectively, with a field of view of $1076'' \times 504''$. The red dashed and white partial circle segments indicate the location and size of the solar disk and the K-Cor occulting disk, respectively.

K-Cor online database.[1] In this study, we assume 0.012 R_{Sun} as the measurement uncertainty, corresponding to the size of two detector pixels. The uncertainties are deduced from ten measurements of a blob position in the K-Cor images. Examples of selected K-Cor blobs are shown in Figure 1. The left panels show the K-Cor blobs at the times of first appearance in K-Cor running difference images. The right panels present their trajectories on K-Cor intensity images during the appearance times. Since the mean solar brightness of K-Cor blobs is about ten times smaller than that of

post-CME rays, it is hard to find the blob structures in K-Cor intensity images. As shown in Figure 1, "Blob-2", "Blob-3", "Blob-6", and "Blob-12" first appear in the post-CME CS at 17:15:00, 17:20:03, and 17:39:16 UT, respectively. They move outward at heights from 1.27 to 1.29 R_{Sun} (Blob-2), from 1.34 to 1.38 R_{Sun} (Blob-3), from 1.65 to 1.73 R_{Sun} (Blob-6), and from 1.38 to 1.54 R_{Sun} (Blob-12). They seem to have irregular "zigzag" trajectories as shown in the enlarged images in the right upper corner of the right column except for the "Blob-2". Here, the "zigzag" trajectories of the blobs can be interpreted as transverse oscillatory motions along the post-CME CS.

Table 1
Instantaneous speed oscillation parameters of 20 K-Cor blobs on 2017 September 10

Blob	T_{first} (UT)	T_{final} (UT)	H_{A} (R_{Sun})	V_{L} (km s^{-1})	# of oscill. cycles	H_{O} (R_{Sun})	P_{I} (sec)	ΔV_{I} (km s^{-1})	W_{I} (R_{Sun})	St_{I}
1	17:12:59	17:15:30	1.37–1.51	674 ($\pm$ 53)	2	1.43	45.5	418	0.02 ($\pm$ 0.008)	0.46 ($\pm$ 0.34)
						1.46	30.5	739	0.02 ($\pm$ 0.012)	0.67 ($\pm$ 0.57)
2	17:15:00	17:16:31	1.27–1.29	151 ($\pm$ 104)	0	-	-	-	-	-
3	17:15:00	17:16:31	1.34–1.38	263 ($\pm$ 104)	1	1.36	46	216	0.02 ($\pm$ 0.006)	1.15 ($\pm$ 0.89)
4	17:20:03	17:22:20	1.36–1.45	423 ($\pm$ 61)	1	1.40	45	264	0.01 ($\pm$ 0.003)	0.37 ($\pm$ 0.46)
5	17:20:03	17:22:20	1.51–1.62	566 ($\pm$ 61)	2	1.54	45	522	0.02 ($\pm$ 0.007)	0.54 ($\pm$ 0.38)
						1.58	30.5	363	0.03 ($\pm$ 0.003)	1.22 ($\pm$ 0.53)
6	17:20:03	17:22:20	1.65–1.73	408 ($\pm$ 61)	2	1.68	60	587	0.03 ($\pm$ 0.008)	0.86 ($\pm$ 0.43)
						1.70	31	189	0.02 ($\pm$ 0.006)	1.08 ($\pm$ 0.74)
7	17:23:05	17:25:22	1.51–1.64	655 ($\pm$ 61)	1	1.55	60	492	0.03 ($\pm$ 0.007)	0.53 ($\pm$ 0.25)
8	17:24:36	17:26:07	1.24–1.29	386 ($\pm$ 104)	1	1.25	30	219	0.02 ($\pm$ 0.007)	1.32 ($\pm$ 0.98)
9	17:28:09	17:31:26	1.29–1.44	526 ($\pm$ 36)	2	1.35	76	317	0.02 ($\pm$ 0.006)	0.37 ($\pm$ 0.25)
						1.38	30.5	434	0.02 ($\pm$ 0.010)	0.80 ($\pm$ 0.64)
10	17:28:54	17:31:41	1.19–1.27	326 ($\pm$ 46)	1	1.23	76	283	0.02 ($\pm$ 0.000)	0.57 ($\pm$ 0.35)
11	17:37:00	17:42:49	1.28–1.74	945 ($\pm$ 16)	3	1.38	91	653	0.03 ($\pm$ 0.005)	0.23 ($\pm$ 0.10)
						1.49	61	420	0.03 ($\pm$ 0.008)	0.36 ($\pm$ 0.18)
						1.58	76	722	0.03 ($\pm$ 0.003)	0.30 ($\pm$ 0.12)
12	17:39:16	17:42:49	1.38–1.54	562 ($\pm$ 33)	3	1.42	45	378	0.02 ($\pm$ 0.006)	0.67 ($\pm$ 0.45)
						1.45	46	494	0.03 ($\pm$ 0.010)	0.81 ($\pm$ 0.42)
						1.48	30	222	0.03 ($\pm$ 0.007)	1.08 ($\pm$ 0.50)
13	17:48:07	17:50:39	1.33–1.44	460 ($\pm$ 52)	1	1.37	75.5	213	0.01 ($\pm$ 0.002)	0.20 ($\pm$ 0.25)
14	17:59:45	18:01:16	1.21–1.27	374 ($\pm$ 104)	1	1.22	31	208	0.03 ($\pm$ 0.009)	2.09 ($\pm$ 1.20)
15	18:04:03	18:08:21	1.40–1.64	660 ($\pm$ 25)	3	1.46	60.5	438	0.02 ($\pm$ 0.005)	0.40 ($\pm$ 0.26)
						1.51	30.5	318	0.01 ($\pm$ 0.000)	0.33 ($\pm$ 0.39)
						1.57	76	214	0.02 ($\pm$ 0.005)	0.22 ($\pm$ 0.14)
16	18:08:51	18:15:11	1.43–1.83	748 ($\pm$ 14)	4	1.50	75.5	240	0.02 ($\pm$ 0.013)	0.27 ($\pm$ 0.24)
						1.56	45.5	161	0.02 ($\pm$ 0.000)	0.43 ($\pm$ 0.26)
						1.62	61	188	0.02 ($\pm$ 0.003)	0.31 ($\pm$ 0.19)
						1.69	76	384	0.03 ($\pm$ 0.007)	0.35 ($\pm$ 0.16)
17	18:10:07	18:12:24	1.19–1.23	182 ($\pm$ 60)	1	1.20	60.5	523	0.03 ($\pm$ 0.004)	1.90 ($\pm$ 1.03)
18	18:31:37	18:35:09	1.27–1.38	343 ($\pm$ 33)	4	1.30	45.5	183	0.03 ($\pm$ 0.007)	1.16 ($\pm$ 0.56)
						1.32	45.5	294	0.02 ($\pm$ 0.010)	0.86 ($\pm$ 0.68)
						1.34	45.5	343	0.02 ($\pm$ 0.006)	0.96 ($\pm$ 0.65)
						1.36	30.5	502	0.02 ($\pm$ 0.012)	1.60 ($\pm$ 1.39)
19	18:32:53	18:35:09	1.38–1.51	692 ($\pm$ 61)	1	1.44	60.5	161	0.03 ($\pm$ 0.007)	0.48 ($\pm$ 0.23)
20	18:51:50	18:55:38	1.25–1.38	348 ($\pm$ 31)	4	1.26	30.5	260	0.02 ($\pm$ 0.006)	1.16 ($\pm$ 0.78)
						1.28	45.5	240	0.02 ($\pm$ 0.003)	0.8 ($\pm$ 0.52)
						1.30	30.5	128	0.03 ($\pm$ 0.003)	1.97 ($\pm$ 0.84)
						1.34	45	903	0.02 ($\pm$ 0.005)	0.95 ($\pm$ 0.62)

T_{first}, T_{final}, H_{A}, V_{L}, H_{O}, P_{I}, ΔV_{I}, W_{I}, and St_{I} represent the first appearance time, final appearance time, appearance height, linear speed during blob propagation, oscillation height, instantaneous oscillation period in the cycle, radial speed amplitudes, lateral width of a blob, and instantaneous Strouhal number, respectively. W_{I} is estimated from the average of the lateral widths of a K-Cor blob during one oscillation period. The errors in V_{L} and St_{I} are measurement errors. The error in W_{I} is the standard deviation.

2.2. Observational Speed Oscillation Parameters of K-Cor Blobs

We identify radial speed oscillations of the 20 K-Cor blobs as follows: (1) We estimate the instantaneous projected speed (V_{I}) of each selected blob in radial direction from the solar disk center by using the following relation: $V_{\mathrm{I}} = (H_{t_1} - H_{t_0})/(t_1 - t_0)$, where $(H_{t_1} - H_{t_0})$ is the observation height of a blob from the solar disk center at t_1 by subtracting the blob height at t_0, and $(t_1 - t_0)$ is the time interval. (2) We construct instantaneous projected speed-time plots for the K-Cor blobs. (3) By visual inspection of the speed-time plots, we carefully check whether or not speed oscillations exist.

Figure 2 presents the height-time variations and instantaneous speed-time variations for four K-Cor blobs

(Blobs 2, 3, 6, and 12). By visual inspection of the speed variations, we find that three blobs (Blobs 3, 6, and 12) seem to undergo at least one oscillation cycle in their instantaneous radial speeds, while one blob (Blob-2) does not have a clear oscillating pattern. The number of oscillation cycle might be one for Blob-3, two for Blob-6, and three for Blob-12. When investigating the projected speed variations of the blobs with at least two oscillation periods (such as Blob-6 and Blob-12), we find that the blobs might have experienced irregular speed oscillations rather than quasi-periodic speed oscillations with constant periods and/or amplitudes. For example, the estimated instantaneous oscillation periods (P_{I}) of Blob-6 are 60 and 31 s, corresponding to the periods of the first and second oscillation cycles, respectively. Their speed amplitudes (ΔV_{I}) are about 587 and 189 km s^{-1},
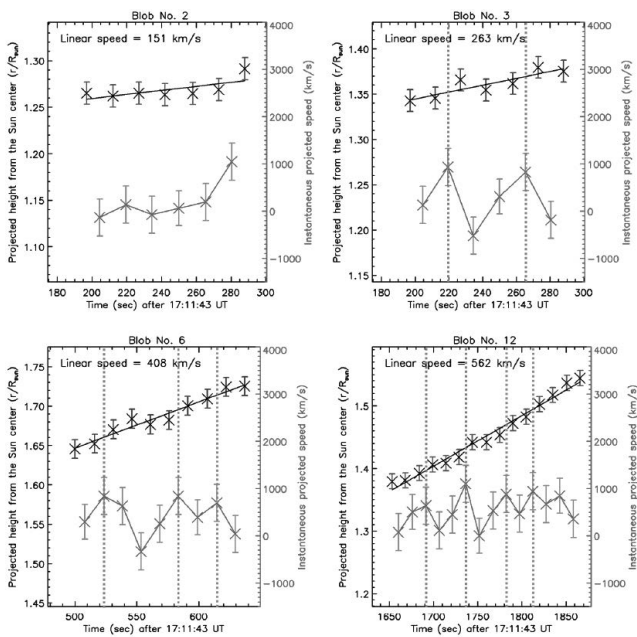
Figure 2. Height-time and instantaneous speed-time plots for the four K-Cor blobs shown in Figure 1. Black crosses indicate the projected height of the local maximum brightness of each blob. The gray vertical error bars show the measurement uncertainties (2 pixels) of blob locations. Black solid lines are linear fits to height-time data. Red crosses indicate the instantaneous projected speed of the local maximum brightness of each blob. The orange vertical error bars show the measurement uncertainties for the instantaneous projected speeds following from linear fits to blob locations. Two blue dotted, blue and green-dotted, and two green dotted vertical lines indicate the first, second, and third oscillation cycles, respectively.

respectively. Here, ΔV_{I} is estimated by using the relation

$$\Delta V_{\mathrm{I}} = \frac{1}{2} \times \left(\frac{V_{I_1} + V_{I_2}}{2} - V_{I_m} \right) \qquad (1)$$

where $(V_{I_1} + V_{I_2})/2$ is the average of the instantaneous speeds at two extreme points during the oscillation period, and V_{I_m} is the minimum (or maximum) value of the projected speeds. If the extreme points are located at crests such as Blob-6, we use the minimum value of the projected speeds as V_{I_m} to estimate ΔV_{I}. By using the same analysis, we estimate P_{I} and ΔV_{I} for all events. The information for our 20 K-Cor blobs and their speed oscillation parameters are summarized in Table 1.

The measurement uncertainty for instantaneous projected speeds is about $400 \ \mathrm{km \, s^{-1}}$ when using the K-Cor temporal cadence (15 s) and given the measurement uncertainties for blob locations ($0.012 \ R_{\mathrm{Sun}}$). Although this uncertainty is similar to, or greater than, ΔV_{I} of each blob and causes difficulties for determining the P_{I} of each blob, the speed oscillations of each blobs are clear visible, as shown in the Figure 2 except for the top-left panel.

We also examine whether or not the radial speed oscillations of K-Cor blobs are similar to the ones of

CME. Since the radial speed amplitudes of CMEs are correlated with the CME speeds and anti-correlated with the periods (Lee et al. 2015, 2018) and the periods are correlated with oscillation heights (Shanmugaraju et al. 2010), we compare these parameters in Figure 3. We then compare the relationships observed for the K-Cor blobs to those from CME observations. We will discuss the similarity and/or dissimilarity of the speed oscillations of post-CME blobs and CMEs in Section 4.

2.3. Observational Strouhal Numbers of K-Cor Blobs

We consider Alfvénic vortex shedding as the possible generation mechanism for the speed oscillations of the post-CME blobs. Vortex shedding is quantified by the Strouhal number (St), which is generally defined as $St = D/(P \times V)$ where D, P, and V are blunt body diameter, the period of vortex shedding, and the speed of the plasma flow, respectively. In fluid dynamics, the Strouhal number is estimated by using the same equation. By using MHD simulations of cylindrical shapes, Gruszecki et al. (2010) show that Strouhal numbers are in the range from 0.15 to 0.25 for different values of plasma-beta, speed, and cylinder diameter. The axis of the cylinder coincides with the direction of the magnetic field in the external medium in those simulations, and the direction of plasma flow is perpendicular to that of the magnetic field, as shown Figure 1 of Gruszecki et al. (2010). By using fluid dynamic experiments, Sakamoto & Haniu (1990) show that Strouhal numbers range from 0.15 to 3.0 for different Reynolds numbers (Re), which is defined as

$$Re = \frac{V \times D}{\nu} \qquad (2)$$

where V, D, and ν are the speed of the plasma flow, blunt body diameter, and the kinematic viscosity of the flow, respectively. Here, the Reynolds number represents the physical condition of the experiment. They also show that the Strouhal number depends on the Reynolds number as shown in their Figures 3 and 4, and that it indicates turbulent motion and vortex shedding patterns as shown in their Figures 6 and 8. To examine whether or not the radial speed oscillations can be explained by vortex shedding, we determine observational Strouhal numbers of the kinematic oscillations of different blobs, and compare our estimates with those from the simulations. Since K-Cor blobs undergo irregular speed oscillations with different speed amplitudes and periods, we estimate the instantaneous Strouhal numbers (St_{I}) defined as

$$St_{\mathrm{I}} = \frac{W_{\mathrm{I}}}{P_{\mathrm{I}} \times V_{\mathrm{L}}} \qquad (3)$$

where W_{I}, P_{I}, and V_{L} are the observed lateral width, speed oscillation period, and linear speed of each K-Cor blob. W_{I} values are estimated by taking the average of lateral widths of a K-Cor blob during one oscillation period. V_{L} is estimated from a linear fit to the time-height data for each blob. We illustrate our procedure for Blob-3 as shown in Figures 1 and 2. W_{I} and P_{I} for
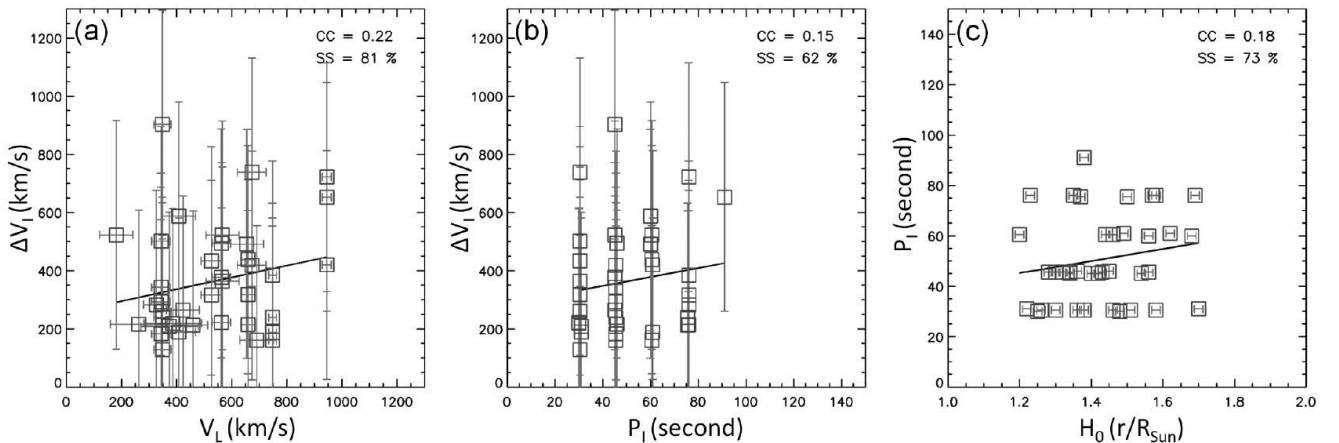
Figure 3. Instantaneous speed amplitude (ΔV_I) of K-Cor blobs as function of (a) linear speed (V_L) and (b) oscillation period (P_I). Panel (c) shows P_I as function of oscillation height H_O. Measurement uncertainties (error bars) are mainly caused by the measurement uncertainties of blob positions. Solid line are linear fits to the data. CC and SS indicate correlation coefficient and statistical significance, respectively; here, the statistical significance is defined as $(1 - p\text{-value}) \times 100$. The p-value, which is the probability of the null hypothesis that both quantities are randomly distributed being true, is estimated by using the number of data and the correlation coefficient under the assumption of Student's t cumulative-distribution function (Neter et al. 1996).

the instantaneous oscillation are 0.02 R_{Sun} and 46 s, respectively. Since V_L is 263 km s^{-1}, St_I is 1.15. We estimate St_I values for all K-Cor blobs; the results are summarized in column 11 of Table 1. We also present their measurement errors caused by the uncertainties in K-Cor blob locations.

3. RESULTS

3.1. Kinematic Oscillations of the Post-CME Blobs

By analyzing the trajectories and instantaneous projected speed-time plots of the 20 K-Cor blobs, we find that all blobs show irregular "'zigzag" trajectories, resembling transverse oscillatory motions along the CS, and that they have at least one oscillatory pattern with periods of about 30–91 s and speed amplitudes of about 128–902 km s^{-1} in their instantaneous radial speeds except for one blob (Blob-2) as shown in the top-right panel of Figure 1. Among those 19 blobs, 10 blobs experience at least two oscillation cycles with different periods and speed amplitudes, while 9 blobs undergo only one oscillation cycle. Our results demonstrate that post-CME blobs generated in a post-CME CS experience apparent radial speed oscillations.

To check the similarity or dissimilarity of the speed oscillations between post-CME blobs and CMEs, we assess the relationships between the radial speed amplitudes of the 19 blobs on the one hand and blob speeds and oscillation periods on the other hand, as shown in Figures 3(a)–(b). We also investigate the relationship between oscillation period and oscillation height in Figure 3(c). We find that the speed amplitude does not correlate with the blob speed (correlation coefficient CC = 0.22) or the period (CC = 0.15). We also find no clear relationship between oscillation period and oscillation height (CC = 0.18). When we only consider the 14 instantaneous speed oscillations which have larger

speed amplitudes than the measurement uncertainty of instantaneous projected speeds in the K-Cor instrument (400 km s^{-1}), we find similar statistical trends: First, there is no relationship between the speed amplitude and the blob speed (CC = −0.04) or the period (CC = −0.03). Second, the period correlates weakly with the oscillation height (CC = 0.18).

3.2. Generation Mechanism of the Kinematic Oscillations of Post-CME Blob

The obtained scaling parameters of the kinematic oscillations of blobs are compared with the results of numerical simulations. We find that the observational Strouhal numbers range from about 0.2 to 2.1 (mean 0.79 and median 0.67). These values are consistent with those (0.15–3.0) from fluid dynamic experiments of bluff spheres in uniform flows (Sakamoto & Haniu 1990), while they are higher than those (0.15–0.25) from MHD simulations of cylindrical shapes (Gruszecki et al. 2010). This might indicate that the radial speed oscillations of post-CME blobs formed in a post-CME CS are caused by fluid dynamic vortex shedding driven by the interaction of the outward-moving blobs with bluff spherical shapes with the background plasma in the post-CME CS. To inspect the relationship between the Strouhal number and the other parameters, we analyze the scatter plots shown in Figures 4(a)–(c). From this, we find that Strouhal numbers correlate stronger with the linear speeds of K-Cor blobs than with the other parameters: CC = −0.70 for linear speeds, CC = −0.61 for oscillation periods, and CC = 0.33 for blob widths. We also find that Strouhal numbers are correlated with the oscillation heights (CC = -0.50, Figure 4(d)), which is caused by the good correlation between the linear speeds and heights as shown in Figure 4 of Paper I. These results indicate that vortex shedding in a post-CME CS is
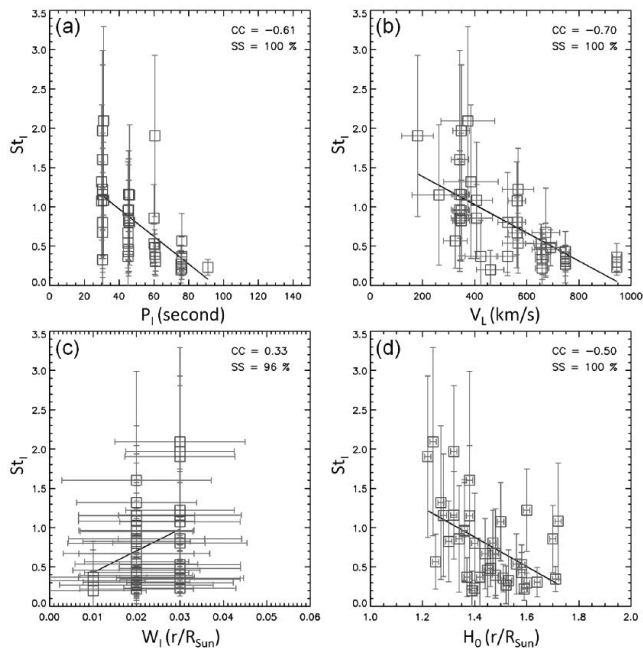
Figure 4. Strouhal number (St_I) as function of (a) oscillation period (P_I), (b) blob linear speed (V_L), (c) blob width (W_I), and (d) oscillation height (H_O). Red symbols indicate 14 instantaneous speed oscillation patterns with speed amplitude larger than than the measurement uncertainty for the instantaneous projected speed in K-Cor data (400 km s^{-1}). Error bars, solid lines, CC, and SS are the same as in Figure 3.
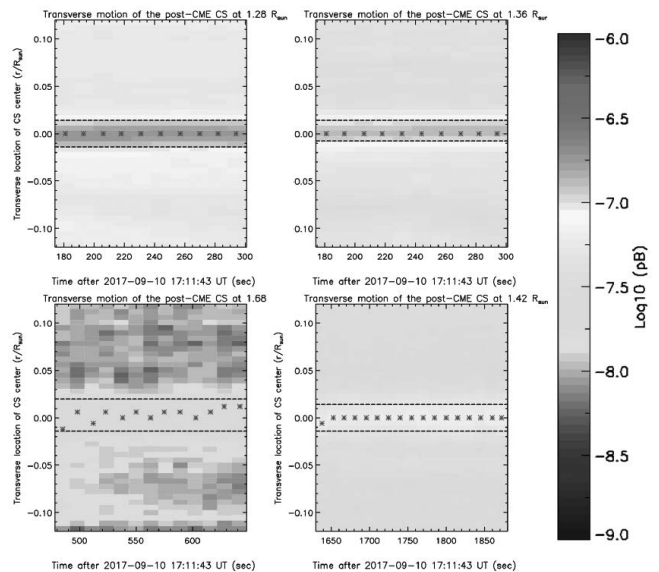

Figure 5. Space-time plots from K-Cor intensity images taken along the cuts marked by purple dotted lines in the right panels of Figure 1 during the appearance of blobs 2, 3, 6, and 12. Star symbols mark maximum pB at each time, indicating the central location of the post-CME CS. The horizontal dashed lines indicate the lateral boundaries of the CS.

mainly controlled by the flow speeds in the post-CME CS. Considering the 14 instantaneous speed oscillation patterns with speed amplitudes larger than the K-Cor measurement uncertainty (red symbols in Figure 4), we find similar statistical trends: First, the observational Strouhal numbers range from about 0.2 to 1.9 (mean 0.74 and median 0.67). Second, we find that Strouhal numbers correlate stronger with the linear speed than with other parameters: CC $= -0.88$ for linear speeds, CC $= -0.59$ for oscillation heights, CC $= -0.41$ for oscillation periods, and CC $= -0.07$ for blob widths.

Since the radial speed oscillations of K-Cor blobs are caused by their transverse oscillatory motions as shown in the right panels of Figure 1, the reader may have a question: the speed oscillations are caused by transverse motions of a post-CME CS such as position angle oscillations as shown in Figure 18 of Ling et al. (2014) or wave-like behavior caused by KHI. The wave-like behavior by KHI is observed in the coronal streamer shown in Figure 3 of Feng et al. (2013). We investigate several possible causes. We first check if the speed oscillations are related to the position angle oscillation of the post-CME CS by examining the transverse variations of the post-CME CS position at the oscillation heights of K-Cor blobs. Figure 5 shows the transverse motions of the post-CME CS at the heights of 1.28, 1.36, 1.68, and 1.42 R_{Sun} during the propagation of Blobs 2, 3, 6, and 12. Here, the heights of 1.36, 1.68, and 1.42 R_{Sun} are related to the first oscillation heights of each K-Cor blob. We do not find any transverse oscillation of

the post-CME CS, while transverse motions and radial speed oscillations of the K-Cor blobs do occur. When examining all events the same way, there is no evidence for a transverse motion of the post-CME CS. Although the central locations of the CS at larger heights seem to slightly change with time (0.006–0.012 R_{Sun}) as shown in the bottom-left panel of Figure 5, this variation is less than or similar to the assumed measurement uncertainty of the K-Cor instrument. We conclude that the radial speed oscillations are not related to the position angle oscillation of the post-CME CS. To check if the speed oscillations are affected by the wave-like behavior of the post-CME CS, we carefully examine whether or not the post-CME CS behaves wave-like as shown in Figure 3 of Feng et al. (2013). By visual inspection of the post-CME CS structures in the K-Cor intensity images during the observations of all K-Cor blobs, we cannot find any wave-like behavior of the post-CME CS structures in the right column of Figure 1. This suggests that the radial speed oscillations are not effected by the KHI.

The above results demonstrate that vortex shedding is a plausible generation mechanism for radial speed oscillations of post-CME blobs formed in a post-CME CS, while it is hard to explain the radial speed oscillations which are caused by either the position angle oscillation of the post-CME CS or the wave-like behavior due to KHI in the post-CME CS.

4. SUMMARY AND DISCUSSION

In this study, we investigate 20 post-CME blobs formed in the post-CME CS observed by K-Cor on 2017 September 10. We search for kinematic oscillations such as zigzagging motions and radial speed oscillations, and
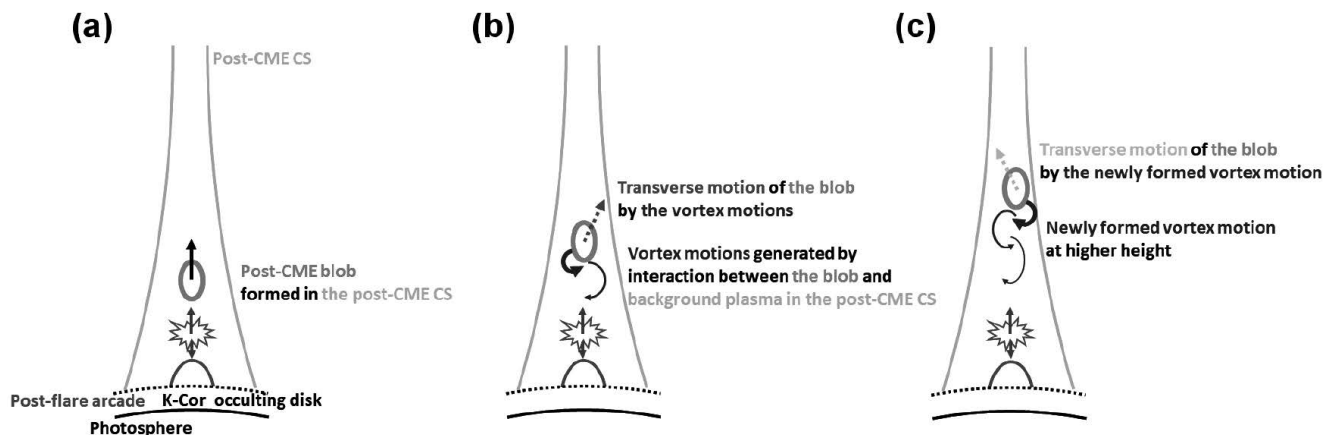
Figure 6. Schematic explanation of the formation of kinematic oscillations of the K-Cor blobs on 2017 September 10. (a) Initial stage, showing the observed locations and apparent motions of a post-CME blob formed in a post-CME CS. (b) Middle stage, representing the apparent vortex motions and the transverse motion of the blob by the vortex motions. (c) Late stage, indicating the newly formed vortex motion at larger height and the transverse motion, which is in opposite direction compared to the transverse motion in the middle stage. During the blob propagation, the blob continuously makes newly formed vortex motions that drive the "zigzag" motion of the blob. A detailed description is provided in the text.

identify a possible generation mechanism for the oscillations. By visual inspection of the trajectories and instantaneous projected speed variations of each K-Cor blob, we find that all blobs except one show irregular "zigzag" trajectories, resembling transverse oscillatory motions along the CS. They each undergo at least one oscillation, with periods ranging from 30 to 91 s and speed amplitudes of 128–902 $km\,s^{-1}$ in their instantaneous radial speeds. Among 19 blobs, 10 blobs experience at least two oscillation cycles with different speed amplitudes and periods, while 9 blobs undergo one oscillation cycle. These results demonstrate that post-CME blobs generated in a post-CME CS experience kinematic oscillations. Our finding regarding the irregular radial oscillation patterns of the 10 blobs is different from CME speed oscillations (Lee et al. 2015; Michalek et al. 2016; Lee et al. 2018), which have quasi-periodic kinematic oscillations in CMEs as shown in Figure 3 of Lee et al. (2015).

To check whether or not the speed oscillations of K-Cor blobs are similar to those of CME, we investigate the relationships between the radial speed amplitudes of the 19 blobs on the one hand and blob speeds and oscillation periods on the other hand. We do not find a correlation of the oscillation amplitude with blob speed (CC = 0.22) or period (CC = 0.15). These results differ from the properties of CME speed oscillation as reported by Lee et al. (2015), who found that the radial speed amplitudes of CMEs are correlated with CME speeds (CC = 0.92) and anti-correlated with the periods in Figure 4 of Lee et al. (2015). We also see no relationship between oscillation periods and oscillation heights (CC = 0.18), which is different from CME speed oscillations as shown by Shanmugaraju et al. (2010) who reported that the period is correlated with oscillation height. From these findings, together with the above finding about the irregular radial oscillation patterns, we infer that

the generation mechanism of speed oscillations in the post-CME blobs is different from that of CMEs.

It is known that "zigzag" motions of buoyant magnetic flux tubes and apparent radial speed oscillations can be caused by Alfvénic vortex shedding (Emonet et al. 2001), and the post-CME CS can provide the conditions needed for generating Alfvénic vortex shedding by interaction between the post-CME blobs and the background plasma. In this study, we consider Alfvénic vortex shedding as a possible generation mechanism for radial speed oscillations. To probe this scenario, we estimate Strouhal numbers by using the observed lateral width, oscillation period, and radial speed of each blob. We then compare our estimates with theoretical and experimental results from MHD simulations and fluid dynamic experiments. We find instantaneous Strouhal numbers ranging from 0.2 to 2.1 (mean 0.79 and median 0.67), which are consistent with those (0.15–3.0) from fluid dynamic experiments of bluff spheres (Sakamoto & Haniu 1990), while they are higher than those (0.15–0.25) from magnetohydrodynamic simulations of cylindrical shapes (Gruszecki et al. 2010). These findings indicate that the kinematic oscillations of post-CME blobs formed in a post-CME CS are caused by fluid dynamic vortex shedding, which is driven by the interaction of outward-moving blobs with bluff spherical shapes with the background plasma. Sakamoto & Haniu (1990) also showed that the Strouhal number depends on the Reynolds number, which indicates turbulent motion, and its vortex shedding pattern. They showed the existence of low-mode ($0.15 \leq St \leq 0.3$) and high-mode ($0.2 \leq St \leq 3.0$) values with Reynolds numbers between 2×10^3 and 2×10^4. Kim & Durbin (1988) showed that high-mode Strouhal number are detectable only in the wake region behind a spherical obstacle, while low-mode numbers can be observed in a much larger region. Our estimated Strouhal numbers for K-Cor blobs (0.2–2.1)

together with the results of Kim & Durbin (1988) imply that the vortex shedding patterns of K-Cor blobs resemble those for Reynolds numbers between 6×10^2 and 10^4, and that they are related to the high-mode Strouhal numbers. The high-mode numbers might be caused by the fact that we can only observe vortex shedding in the wake region behind the post-CME blobs with the K-Cor instrument.

Combining our results with previous observations of magnetic reconnection regions and post-CME blob formation (Cheng et al. 2018; Lee et al. 2020; Yu et al. 2020), we propose a schematic model for the formation of the kinematic oscillations of the K-Cor blobs on 2017 September 10 which we illustrate in Figure 6. The observed kinematics can be explained through the following process: (1) Initially, a post-CME blob is triggered by a tearing mode instability near the middle of the post-CME CS and propagates outward along the CS as shown in Figure 6(a). The outward motion might be driven by the reconnection outflows generated by magnetic reconnection processes in the CS. (2) During its propagation, the blob makes vortex motions in the post-CME CS as shown in Figure 6(b). The vortex motions are generated by the interaction between the blob and the background plasma in the CS, and they cause a transverse motion of the blob. (3) The blob continuously makes newly formed vortex motion at larger heights. The newly formed vortex motion drives the transverse motion toward the direction opposite to the direction of the transverse motion. The shedding of the vortex motions from the alternate sides of the blob cause the "zigzag" motion of the blob, resulting in apparent radial speed oscillation in the instantaneous projected speed-time plot.

Our inner corona observations with K-Cor having high spatial resolution (5.5 arcsec/pixel) and temporal cadence (15 s) show for the first time observational evidence for kinematic oscillations of post-CME blobs in a post-CME CS, and that the oscillations might be generated by the vortex motions caused by the interaction between the blob and its background plasma. These results, together with high resolution MHD simulations (Mei et al. 2012), might help understanding the turbulent motions of post-CME blobs inside a post-CME CS. We suggest that high spatial resolution and high temporal cadence images are needed to understand the evolution of small scale coronal structures and their kinematics in the inner corona.

Aᴄᴋɴᴏᴡʟᴇᴅɢᴍᴇɴᴛꜱ

Rᴇꜰᴇʀᴇɴᴄᴇꜱ

Brueckner, G. E., Howard, R. A., Koomen, M. J., et al. 1995, The Large Angle Spectroscopic Coronagraph (LASCO), Sol. Phys., 162, 357

Chae, J., Cho, K., Kwon, R.-Y., et al. 2017, Evidence for a Magnetic Reconnection Origin of Plasma Outflows along Post-CME Rays, ApJ, 841, 49

Cheng, X., Li, Y., Wan, L. F., et al. 2018, Observations of Turbulent Magnetic Reconnection within a Solar Current Sheet, ApJ, 866, 64

Emonet, T., Moreno-Insertis, F., & Rast, M. P. 2001, The Zigzag Path of Buoyant Mangetic Tubes and the Generation of Vorticity along Their Periphery, ApJ, 549, 1212

Feng, L., Inhester, B., & Gan, W. Q. 2013, Kelvin-Helmholtz Instability of a Coronal Streamer, ApJ, 774, 141

Furth, H. P., Killeen, J., & Rosenbluth, M. N. 1963, Finite-Resistivity Instabilities of a Sheet Pinch, Phys. Fluids, 6, 459

Gary, D. E., Chen, B., Dennis, B. R., et al. 2018, Microwave and Hard X-Ray Observations of the 2017 September 10 Solar Limb Flare, ApJ, 863, 83.

Gopalswamy, N., Yashiro, S., Mäkelä, P., et al. 2018, Extreme Kinematics of the 2017 September 10 Solar Eruption and the Spectral Characteristics of the Associated Energetic Particles, ApJL, 863, L39

Gruszecki, M., Nakariakov, V. M., van Doorsselaere, T., & Arber, T. D. 2010, Phenomenon of Alfvénic Vortex Shedding, Phys. Rev. Lett., 105, 055004

Guo, L.-J., Bhattacharjee, A., & Huang, Y.-M. 2013, Distribution of Plasmoids in Post-Coronal Mass Ejection Current Sheets, ApJL, 771, L14

Howard, R. A., Moses, J. D., Vourlidas, A., et al. 2008, Sun Earth Connection Coronal and Heliospheric Investigation (SECCHI), SSRv, 136, 67

Kim, H. J., & Durbin, P. A. 1988, Observations of the Frequencies in a Sphere Wake and of Drag Increase by Acoustic Excitation, Phys. Fluids, 31, 3260

Ko, Y.-K., Raymond, J. C., Lin, J., et al. 2003, Dynamical and Physical Properties of a Post-Coronal Mass Ejection Current Sheet, ApJ, 594, 1068

Krall, J., Chen, J., Duffin, R. T., Howard, R. A., & Thompson, B. J. 2001, Erupting Solar Magnetic Flux Ropes: Theory and Observation, ApJ, 562, 1045

Kwon, R.-Y., Vourlidas, A., & Webb, D. 2016, Three-Dimensional Geometry of a Current Sheet in the High Solar Corona: Evidence for Reconnection in the Late Stage of the Coronal Mass Ejections, ApJ, 826, 94

Lee, H., Moon, Y.-J., & Nakariakov, V. M. 2015, Radial and Azimuthal Oscillations of Halo Coronal Mass Ejections in the Sun, ApJL, 803, L7.

Lee, H., Moon, Y.-J., Nakariakov, V. M., et al. 2018, Three-dimensional Oscillations of 21 Halo Coronal Mass Ejections Using Multi-spacecraft Data, ApJ, 868, 18

Lee, J., Cho, K.-S., Lee, K., et al. 2020, Formation of Post-CME Blobs Observed by LASCO-C2 and K-Cor on 2017 September 10, ApJ, 892, 129

Lin, J., & Forbes, T. G. 2000, Effects of Reconnection on the Coronal Mass Ejection Process, J. Geophys. Res., 105, 2375

Lin, J., 2002, Energetics and Propagation of Coronal Mass Ejections in Different Plasma Environments, Chin. J. Astron. Astrophys., 2, 539

Lin, J., Ko, Y.-K., Sui, L., et al. 2005, Direct Observations of the Magnetic Reconnection Site of an Eruption on 2003 November 18, ApJ, 622, 1251

Lin, J., Murphy, N. A., Shen, C., et al. 2015, Review on Current Sheets in CME Development: Theories and Observations, Space Sci. Rev., 194, 237

Ling, A. G., Webb, D. F., et al. 2014, Development of a Current Sheet in the Wake of a Fast Coronal Mass Ejection, ApJ, 784, 91

Liu, W., Jin, M., Downs, C., et al. 2018, A Truly Global Extreme Ultraviolet Wave from the SOL2017-09-10 X8.2+ Solar Flare-Coronal Mass Ejection, ApJL, 864, L24

Liu, Y. D., Zhu, B., & Zhao, X. 2019, Geometry, Kinematics, and Heliospheric Impact of a Large CME-driven Shock in 2017 September, ApJ, 871, 8

Longcope, D., Unverferth, J., Klein, C., et al. 2018, Evidence for Downflows in the Narrow Plasma Sheet of 2017 September 10 and Their Significance for Flare Reconnection, ApJ, 868, 148

Mei, Z., Shen, C., Wu, N., et al. 2012, Numerical Experiments on Magnetic Reconnection in Solar Flare and Coronal Mass Ejection Current Sheets, MNRAS, 425, 2824

Michalek, G., Shanmugaraju, A., Gopalswamy, N., et al. 2016, Statistical Analysis of Periodic Oscillations in LASCO Coronal Mass Ejection Speeds, Sol. Phys., 291, 3751

Nakariakov, V. M., Aschwanden, M. J., & Van Doorsselaere, T. 2009, The Possible Role of Vortex Shedding in the Excitation of Kink-Mode Oscillations in the Solar Corona, A&A, 615, A143

Neter, J., Kutner, M. H., Wasserman, W., & Nachtsheim, C. 1996, Applied Linear Statistical Models, 4th edn. (New York: McGraw-Hill/Irwin)

Nistico, G., Vladimirov, V., Nakariakov, V. M., et al. 2018, Oscillations of Cometary Tails: A Vortex Shedding Phenomenon?, A&A, 502, 661

Riley, P., Lionello, R., Mikić, Z., et al. 2007, Bursty Reconnection Following Solar Eruptions: MHD Simulations and Comparison with Observations, ApJ, 655, 591

Sakamoto, H., & Haniu, H. 1990, A Study on Wortex Shedding From Spheres in a Uniform Flow, J. Fluids Engineer., 112, 386

Samanta, T., Tian, H., & Nakariakov, V. M. 2019, Evidence for Vortex Shedding in the Sun's Hot Corona, Phys. Rev. Lett., 123, 035102

Shanmugaraju, A., Moon, Y.-J., Cho, K.-S., et al. 2010, Quasi-Periodic Oscillations in LASCO Coronal Mass Ejection Speeds, ApJ, 708, 450

Shen, C., Lin, J., & Murphy, N. A. 2011, Numerical Experiments on Fine Structure within Reconnecting Current Sheets in Solar Flares, ApJ, 737, 14

Shibata, K., & Tanuma, S. 2001, Plasmoid-Induced-Reconnection and Fractal Reconnection, Earth Planets Space, 53, 473

Song, H. Q., Kong, X. L., Chen, Y., et al. 2012, A Statistical Study on the Morphology of Rays and Dynamics of Blobs in the Wake of Coronal Mass Ejections, Sol. Phys., 276, 261

Syntelis, P., & Antolin, P. 2019, Kelvin-Helmholtz Instability and Alfvénic Vortex Shedding in Solar Eruptions, ApJL, 884, L4

Takahashi, T., Qiu J., Shibata, K., et al. 2017, Quasi-periodic Oscillations in Flares and Coronal Mass Ejections Associated with Magnetic Reconnection, ApJ, 848, 102

Tritton, D. J. 1977, Physical Fluid Dynamics, 1st edn. (London: van Nostrand Reinhold)

Vršnak, B., Poletto, G., Vujić, E., et al. 2009, Morphology and Density Structure of Post-CME Current Sheets, A&A, 499, 905

Warren, H. P., Brooks D. H., Ugarte-Urra, I., et al. 2018, Spectroscopic Observations of Current Sheet Formation and Evolution, ApJ, 854, 122

Webb, D. F., Burkepile, J., Forbes, T. G., et al. 2003, Observational evidence of new current sheets trailing coronal mass ejections, J. Geophys. Res., 108, 1440

Webb, D. F., & Vourlidas, A. 2016, LASCO White-Light Observations of Eruptive Current Sheets Trailing CMEs, Sol. Phys., 291, 3725

Williamson, C. H. K., 1996, Vortex Dynamics in the Cylinder Wake, Annu. Rev. Fluid Mech., 28, 477

Yu, S., Chen, B., Reeves, K.K., et al. 2020, Magnetic Reconnection During the Post-Impulsive Phase of a Long-Duration Solar Flare: Bi-Directional Outflows as a Cause of Microwave and X-ray Bursts, ApJ, 900, 1